

NNT : ***

n°LAL : ***

Thèse de doctorat

Search of the $0\nu\beta\beta$ decay with the SuperNEMO demonstrator

Thèse de doctorat de l'Université Paris-Saclay
préparée à l'Université Paris Saclay au sein du Laboratoire Irène-Joliot Curie
(anciennement Laboratoire de l'Accélérateur Linéaire)

École doctorale n°576 Particles, Hadrons, Energy, Nuclei, Instrumentation,
Imaging, Cosmos et Simulation (PHENIICS)
Spécialité de doctorat : Physique des particules

Thèse présentée et soutenue à Orsay, le ***, par

CLOÉ GIRARD-CARILLO

Composition du Jury :

Président

Rapporteur

Rapporteur

Christine Marquet
CENBG - Bordeaux-Gradignan

Examineur

Examineur

Examineur

Laurent Simard
LAL - Orsay

Directeur de thèse

Mathieu Bongrand
LAL - Orsay

Co-directeur de thèse

Contents

Contents	3
Introduction	7
1 Phenomenology of particle physics	9
1.1 The Standard Model of particle physics	9
1.1.1 Bosons	9
1.1.2 Fermions	9
1.1.3 $2\nu\beta\beta$ decay	9
1.1.4 Where the Standard Model ends	9
1.2 Going beyond the Standard Model with neutrinos	9
1.2.1 Neutrino flavors and oscillations	9
1.2.2 Neutrino masses and nature	9
1.2.3 Other searches beyond the Standard Model with neutrinos	9
2 $0\nu\beta\beta$ experiment status	11
2.1 Experimental design criteria	11
2.1.1 Aspects of the nuclear matrix elements	12
2.1.2 Quenching	12
2.2 $0\nu\beta\beta$ direct search experiments	12
2.2.1 Semiconductors	12
2.2.2 Bolometers	13
2.2.3 Time projection chambers	13
2.2.4 Scintillators	16
2.2.5 Tracking calorimeters	16
3 The SuperNemo demonstrator	17
3.1 The SuperNemo demonstrator	17
3.1.1 Comparison with Nemo3 experiment	17
3.1.2 Experimental design	17
3.1.3 Sources	17
3.1.4 Tracker	17
3.1.5 Calorimeter	17

3.1.5.1	Scintillator	17
3.1.5.2	Photomultiplier	17
3.1.6	Calibration systems	17
3.1.7	Control Monitoring system	17
3.1.8	Electronics	17
3.2	The background of SuperNEMO	17
3.2.1	Internal background	17
3.2.2	External background	18
3.2.3	Background specifications	18
3.2.4	Measured demonstrator background levels	18
3.3	Magnetic field	18
3.4	The SuperNemo software	18
3.4.1	Simulation	18
3.4.2	Reconstruction	18
4	Analysis tools	19
4.1	Internal and external probabilities	19
4.1.1	Internal probability	19
4.2	Simulations	20
4.2.1	Modifications of simulation software	20
4.2.2	Internal background simulations	20
4.2.3	$0\nu\beta\beta$ simulations	20
5	Detector commissioning	21
5.1	Reflectometry analysis	21
5.1.1	Goal of the reflectometry analysis	21
5.1.2	Pulse timing: controlling cable lengths	22
5.1.3	Signal attenuation	27
5.1.4	Pulse shape analysis	29
5.1.5	Comparison with ^{60}Co	29
5.1.6	Conclusion	29
5.2	Calibrating the electronic boards	29
5.2.1	Principle	29
5.2.2	Measuring the time offset of front end boards	29
5.2.3	Results	29
5.3	Energy calibration of optical modules	29
5.4	Baseline studies	29
5.5	Light Injection System	29
6	Characterisation of the calorimeter time resolution	31
6.1	Interaction of particles in the SuperNEMO scintillators	32
6.1.1	Interaction of electrons	32
6.1.2	Interaction of photons	32
6.2	Measurement of the time resolution with a ^{60}Co source	33
6.2.1	Description of Cobalt 60 nucleus	34
6.2.2	Time response of optical modules	34
6.2.3	Final experimental design	37

6.2.4	Signal events selection	39
6.2.5	Background estimation	41
6.2.6	Detector efficiency	45
6.2.7	Determination of the individual timing resolution of each optical module	46
6.2.8	Conclusion	50
6.3	The Light Injection System	50
6.3.1	Light injection system commissioning	51
6.3.2	Time resolution of optical modules	51
7	Sensitivity of the SuperNEMO demonstrator to the $0\nu\beta\beta$	53
7.1	The $0\nu\beta\beta$ Signal and background model	53
7.1.1	The $0\nu\beta\beta$ signal	54
7.1.2	Inside detector backgrounds	55
7.1.2.1	Internal backgrounds	55
7.1.2.2	Tracker contamination by natural isotopes	55
7.1.3	Outside detector backgrounds	56
7.2	Event selection	56
7.3	Demonstrator sensitivity to the Selenium-82 $0\nu\beta\beta$ decay	58
7.4	Impact of sources contamination levels on the sensitivity	60
7.4.1	Influence of the contamination levels	61
7.4.2	Optimisation of the event selection	63
7.5	Influence of the magnetic field	67
7.6	The 25 Gauss magnetic field	67
7.6.1	Influence of the magnetic field on optical modules and reconstruction efficiency	67
7.6.2	Simulations of the magnetic field inside the demonstrator and reconstructed track fit	68
7.7	Searching for the Neodymium-150 $0\nu\beta\beta$ decay	68
7.8	The final detector sensitivity	69
7.9	Conclusion	70
8	Improvement of the rejection of the internal Thallium-208 background	71
8.1	Motivations for this study	71
8.1.1	The internal ^{208}Tl background	71
8.1.2	Rejection of the ^{208}Tl background	72
8.2	Describe mathematically internal events	73
8.2.1	The internal probability	73
8.2.2	The exponential probability	74
8.3	Event selection	74
8.4	Impact of ^{208}Tl rejection on the experiment's sensitivity	74
8.4.1	Influence of the calorimeter time resolution	74
8.5	Conclusions	75
	Conclusion	77

Bibliography	79
---------------------	-----------

Sensitivity of the SuperNEMO demonstrator to the $0\nu\beta\beta$

In this chapter, we present a study aiming to evaluate the SuperNEMO's sensitivity to the $0\nu\beta\beta$ decay, and the corresponding effective neutrino mass. Studies of this kind have already been conducted, and the final detector is expected to exclude half-lives up to 1.2×10^{26} y (90% CL), with an exposure of 500 kg.y for the ^{82}Se ¹ [8]. In 2015 began the demonstrator installation at the Laboratoire Souterrain de Modane, aiming to assess the feasibility of such a large scale detector based on the NEMO-3 technology. With an exposure of 17.5 kg.y, the demonstrator could reach a sensitivity on the $0\nu\beta\beta$ process of 5.3×10^{24} y (90% CL) [9].

At the time of the current analysis, the coil, which is supposed to deliver a magnetic field inside the detector, was not yet installed on the demonstrator. We aim to explore the impact, on both the demonstrator and final detector sensitivity, of the presence of this magnetic field. The findings of this study will participate in the final decision on the installation of the coil. In a context of investigating the demonstrator and final detector's capabilities, different internal source contamination levels are considered. The topology of interest is the two electrons ($2e$) topology, and we use the total energy sum to discriminate the signal from the background events. Thanks to SuperNEMO tracking capabilities, topological informations are also exploited to improve the sensitivity.

- parler des autres isotopes qu'on voudrait mettre

7.1 The $0\nu\beta\beta$ Signal and background model

A full simulation for the demonstrator was performed, in order to determine the upper limit on $0\nu\beta\beta$ half-life that can be probed with SuperNEMO. This sensitivity greatly depends on the number of background events detected but non-rejected during the data taking. The expected number of events for natural isotopes depend on their activities inside the source foils (for Thallium-208 and Bismuth-214), or on the tracker's wires (for Radon-222 decaying in Bismuth-214). It was necessary,

¹Supposing Selenium-82 $0\nu\beta\beta$ decays through the exchange of a light Majorana neutrino.

during the design of the detector, to constrain their maximal tolerable activities, to guarantee a high sensitivity to the $0\nu\beta\beta$ disintegration [10]. These values are given in the table, per disintegration unit per second, for one kg of source material, or for one m^3 of gas inside the tracker.

Meanwhile, the amount of expected $2\nu\beta\beta$ decays is mainly driven by its $T_{1/2}^{2\nu}$ value: the higher the half-life of this process, the lower its contribution in the total number of expected background. For Selenium-82 sources, we take the $2\nu\beta\beta$ half-life measured by NEMO-3, $T_{1/2}^{2\nu} = 9.39 \pm 0.17$ (stat) ± 0.58 (syst) $\times 10^{19}$ years [11].

In the Tab. 7.1 is summarised the expected number of signal and background events, both for the SuperNEMO demonstrator and final detector. We also present, for each of the process, the amount of simulated events. The figures in the central

Type of decay	Expected decays		Simulated decays
	Demonstrator	Final detector	
$0\nu\beta\beta$ ($T_{1/2}^{0\nu} = 2.5 \cdot 10^{23}$ y)	$3.6 \cdot 10^2$	$1.0 \cdot 10^4$	$1.0 \cdot 10^7$
$2\nu\beta\beta$ ($T_{1/2}^{2\nu} = 9.39 \times 10^{19}$ y)	$9.5 \cdot 10^5$	$2.7 \cdot 10^7$	$1.0 \cdot 10^7$
^{208}Tl ($\mathcal{A}^{\text{Tl}} = 10 \mu\text{Bq/kg}$)	$5.5 \cdot 10^3$	$1.6 \cdot 10^5$	$1.0 \cdot 10^7$
^{214}Bi ($\mathcal{A}^{\text{Bi}} = 2 \mu\text{Bq/kg}$)	$1.1 \cdot 10^3$	$3.1 \cdot 10^4$	$1.0 \cdot 10^7$
^{222}Rn ($\mathcal{A}^{\text{Rn}} = 0.15 \text{ mBq/m}^3$)	$1.8 \cdot 10^5$	$7.2 \cdot 10^6$	$1.0 \cdot 10^8$

Table 7.1: Expected and simulated decays for different processes, both for the demonstrator (17.5 kg.y) and for the final detector exposures (500 kg.y), assuming target background activities are reached: $\mathcal{A}^{\text{Tl}} = 10 \mu\text{Bq/kg}$, $\mathcal{A}^{\text{Bi}} = 2 \mu\text{Bq/kg}$, $\mathcal{A}^{\text{Rn}} = 0.15 \text{ mBq/m}^3$. The measured half-life $T_{1/2}^{2\nu} = 9.39 \times 10^{19}$ y for Selenium-82's $2\nu\beta\beta$ is taken, and we assume $T_{1/2}^{0\nu} = 2.5 \times 10^{23}$ y [11].

column represent the total number of disintegrations, without taking into account any technique to reject background, and for the total energy window.

Nevertheless, the number of decays presented in the table are expected to be extremely reduced, notably by the application of event selections aimed at maximising the sensitivity to the excluded $0\nu\beta\beta$ half-life (Sec. 7.2). Moreover, this effect is augmented by the fact that, for the current sensitivity analysis, we will focus on a narrow energy window, called *region of interest*, whose usefulness will be described in more detail in Sec. 7.3. Therefore, to properly conduct this sensitivity study, it was necessary to simulate a large number of events, so that the signal and backgrounds are correctly represented in the region of interest. Let us now detail the simulations produced as part of this analysis.

7.1.1 The $0\nu\beta\beta$ signal

The SuperNEMO detector was designed to search for the never-observed $0\nu\beta\beta$ decay. In the following, we assume the underlying mechanism for this decay is the exchange of a light Majorana neutrino, the so-called mass mechanism (MM), as it is the most widespread mechanism. The hypothetical $0\nu\beta\beta$ signal would be detected

as an excess of events in the region of interest, with respect to the predicted background contamination level. Some 10^7 $0\nu\beta\beta$ events were simulated inside the source foils, using the DECAY0 software [12]. The simulations are normalised assuming the half-life excluded by NEMO-3, $T_{1/2}^{0\nu} = 2.5 \cdot 10^{23}$ y (90% CL) [11].

7.1.2 Inside detector backgrounds

In addition with the $0\nu\beta\beta$ decay, we simulated different types of backgrounds, that could mimic the searched signal.

7.1.2.1 Internal backgrounds

The so-called *internal backgrounds* stand for decays occurring inside the source foils, presenting the same signature as the $0\nu\beta\beta$ signal. These backgrounds, already introduced earlier, are the $2\nu\beta\beta$ of the source isotope, as well as disintegrations of ^{208}Tl and ^{214}Bi .

The $2\nu\beta\beta$ process

In the full energy range, the allowed $2\nu\beta\beta$ decay stands as the dominant internal background type. Its total energy spectrum is a continuum, whose ending point should stand at $Q_{\beta\beta} = 2.99$ MeV, but is slightly increased by the detector's energy resolution. We simulated 10^7 events of this decay inside the source foils, in the full energy window. However, above a certain energy value, the number of $2\nu\beta\beta$ events decreases very quickly. To offset this effect, we simulated additional 10^7 of this decay on a slightly lower energy range, that is to say above 2 MeV. The second set of simulations is normalised with the first one. In this way, the lack of $2\nu\beta\beta$ simulated events in the high-energy tail is avoided, without requiring too high computational resources.

Source foils contamination by natural isotopes

As described in Sec. 3.2.1, after sources purification, remaining natural isotopes such as ^{208}Tl or ^{214}Bi can still be present inside the foils. This class of contamination constitutes the principal internal source of background, with the $2\nu\beta\beta$ decay. We simulated 10^7 decays both for the two isotopes, inside the source foils.

7.1.2.2 Tracker contamination by natural isotopes

The presence of gaseous Radon-222 inside the tracker, mainly deposited on the copper wires, can produce events similar to internal one. In fact, one of the progeny of Radon-222, the Bismuth-214, can decay on (or near) a foil, and appear with a $2e$ topology, becoming hard to distinguish from a double beta decay candidate. As this isotope is distributed throughout the whole tracking detection volume, to study the experiment's sensitivity, we simulated a large quantity of this decay on the tracker wires. This way, we maximise the amount of ^{214}Bi events, coming from ^{222}Rn decays, in the region of interest.

7.1.3 Outside detector backgrounds

This background category is populated by the external γ -ray flux produced by radioactive isotope decays in detector components or surrounding laboratory rocks, as well as neutron interactions in the shield. The most notorious difference is the fact that the SuperNEMO scintillator blocks are thicker than those of NEMO-3. Therefore, a gamma is more likely to be detected and therefore, in that case, the event would not contribute to the background in the $2e$ channel. As a consequence, for the same PMTs radioactivity, the external gamma background rate is expected to be less important for the SuperNEMO demonstrator than for NEMO-3. Moreover, radiopurity measurements of SuperNEMO PMTs allow to conclude that their total activity is better than for those of NEMO-3, for the two principal considered isotopes ^{208}Tl and ^{214}Bi [13]. The NEMO-3 experiment set a limit on the external background number of counts, of < 0.2 events in the $2e$ topology, for the energy range $[2.8; 3.2]$ MeV (two electrons energy sum), for an exposure of $34.3 \text{ kg}\cdot\text{y}$, with ^{100}Mo sources [14]. Given the fact that SuperNEMO is expected to be better than NEMO-3 at rejecting external background events, we consider that all external backgrounds from outside the foil, apart from ^{222}Rn in the tracking volume, are expected to be negligible, and were not simulated. Even if the regions of interest are slightly different between these two experiments, it produces negligible increase on the external background contribution.

In the following we present an optimisation of the event selection that has been set up to maximise the excluded $0\nu\beta\beta$ half-life in this specific topology.

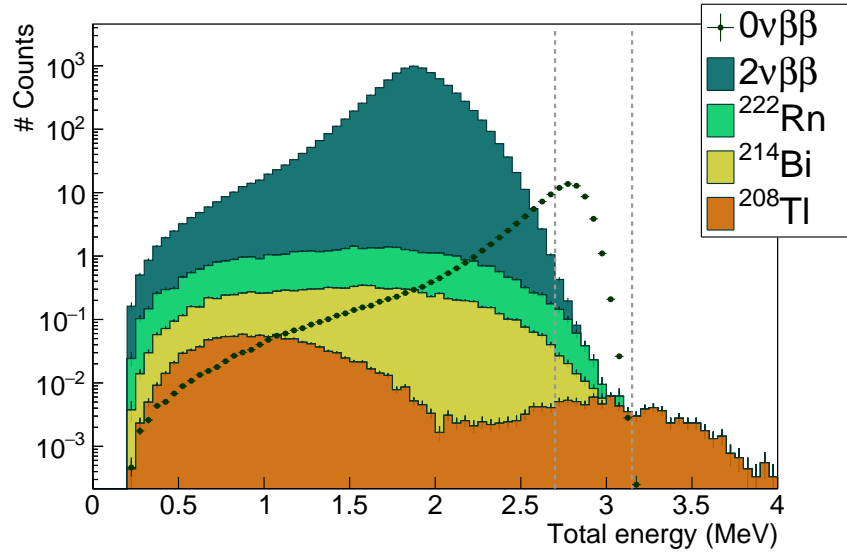
7.2 Event selection

For SuperNEMO, the $0\nu\beta\beta$ signature is two-electrons events, emitted simultaneously from the same vertex on the source foils, with an energy sum compatible with $Q_{\beta\beta} = 2.99 \text{ MeV}$ for the Selenium-82. Therefore, we conducted this analysis selecting only events matching the $2e$ topology, where a reconstructed particle is tagged as an electron if it has

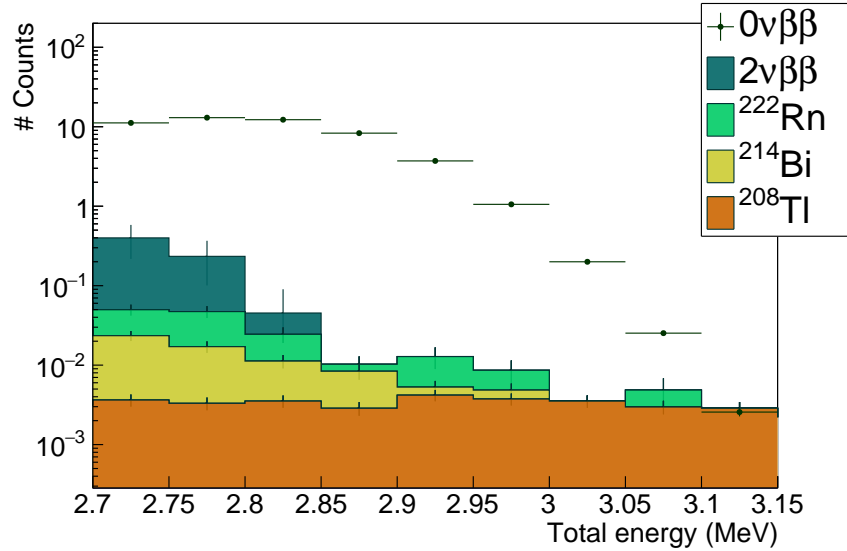
- a vertex on the source foils,
- a reconstructed track inside the wire chamber,
- and an associated calorimeter hit.

All these selections represent the so-called *first order cuts*.

We present the total energy spectra for each simulated process, after event selection, in Fig. 7.1. The $0\nu\beta\beta$ spectrum is peaked around 2.8 MeV, as the available energy $Q_{\beta\beta} = 2.99 \text{ MeV}$ is degraded by electron energy losses before reaching the calorimeter (mainly inside the dense source material, as well as inside the wire chamber), explaining the asymmetric energy distribution. Whatever their origin, either Radon-222 contaminations inside the tracker gas, or internal contaminations of the source foils, the Bismuth-214 energy distributions have nearly the same shape. Moreover, a great part of Radon-222 events have been rejected by the topological cuts. Therefore, given the activities of ^{222}Rn in



(a)



(b)

Figure 7.1: Total energy spectra for the $0\nu\beta\beta$ signal and main backgrounds, for (a) the full energy range, and (b) for the $[2.7; 3.15]$ MeV energy range, whose optimisation is discussed in Sec. 7.3.

the tracker and ^{214}Bi inside the source foils, these two background types both contribute at the same level in the full energy range. The ^{208}Tl energy distribution reveals the internal conversion of the 2.614 MeV gamma, emitted after ^{208}Tl β^- disintegrations.

In what follows, we explain the steps that allowed to give a $T_{1/2}^{0\nu}$ sensitivity for the demonstrator.

- dire aussi que là on présente pour Se avec champ. Du coup ya la coupure du premier ordre sur la courbure de la trace aussi.

7.3 Demonstrator sensitivity to the Selenium-82 $0\nu\beta\beta$ decay

The two-electrons energy sum for the $0\nu\beta\beta$ is expected as a peak at the end point of the $2\nu\beta\beta$ energy distribution. This energy peak would be degraded by electron energy losses inside the source foils and wire chamber, as well as by the calorimeter energy resolution. In Fig. 7.1 is represented, for specific data taking conditions, the energy spectra of the $0\nu\beta\beta$ decay, assuming $T_{1/2}^{0\nu} = 2.5 \times 10^{23}$ years. The enlarged peak we are discussing is clearly noticeable around 2.7 MeV. A widespread technique consists in constraining the $0\nu\beta\beta$ decay searches to a narrow energy range, the so-called *region of interest* (ROI), materialised by the two vertical dashed lines. In the following, we expose general principles leading to determination of the best limit on $T_{1/2}^{0\nu}$, in the appropriate region of interest. The reasoning presented is valid for all cases (all exposures, internal contamination levels and field conditions). Nevertheless, we illustrate the method by presenting the results for the specific case were of the demonstrator (Selenium-82 sources, 17.5 kg/y exposure), with the specified internal contamination levels ($\mathcal{A}^{\text{Tl}} = 10 \mu\text{Bq/kg}$ and $\mathcal{A}^{\text{Bi}} = 2 \mu\text{Bq/kg}$).

In case of the non-observation of a $0\nu\beta\beta$ signal, the expected upper limit on the half-life is provided for a given $[E_{\min}; E_{\max}]$ energy range, and depends on the characteristics of the detector. First, it depends on the signal detection efficiency $\epsilon_{0\nu}$ in this energy window, secondly on the source isotope nature, as well as the detector's exposure $m \times t$. It follows

$$T_{1/2}^{0\nu} > \frac{\mathcal{N}_A \ln 2}{M} \times \frac{\epsilon_{0\nu} \times m \times t}{N_{0\nu}^{\text{excl.}}}, \quad (7.1)$$

with \mathcal{N}_A the Avogadro number, m the quantity of isotope in the source foils, M its molar mass, and t the total time of data taking. $N_{0\nu}^{\text{excl.}}$ is the number of signal events excluded, calculated with the Feldman-Cousins statistics from the total expected number of background events.

The Feldman-Cousins statistics [16] is a wide-used method in rare events search experiments, providing confidence intervals for upper limits in the case of Poisson processes with background. We use this method in the framework of this analysis to provide a limit, at 90% CL, on the number of expected signal events $N_{0\nu}^{\text{excl.}}$, on the basis of the expected number of background events, given below.

- The $2\nu\beta\beta$ background

In Eq. (7.1), we defined the upper limit on $T_{1/2}^{0\nu}$ from the number of excluded signal events, and the signal selection efficiency $\epsilon_{0\nu}$. The same way, we can define the number of observed $2\nu\beta\beta$ events $N_{2\nu}$ from the half-life $T_{1/2}^{2\nu}$ and the $2\nu\beta\beta$ selection efficiency $\epsilon_{2\nu}$,

$$N_{2\nu} = \frac{\mathcal{N}_A \ln 2}{M} \times \frac{\epsilon_{2\nu} \times m \times t}{T_{1/2}^{2\nu}}. \quad (7.2)$$

- Natural radioactive backgrounds

We consider the background massic activities $A_{\text{rad.}}$, and $\epsilon_{\text{rad.}}$ their selection

efficiencies in a given energy window. The number of background events is therefore given, for the ^{208}Tl and ^{214}Bi internal contaminations, as

$$N_{\text{rad.}} = A_{\text{rad.}} \epsilon_{\text{rad.}} \times m \times t \quad (7.3)$$

where $A_{\text{rad.}}$ is given in Bq/kg. Similarly, for the ^{222}Rn background,

$$N_{\text{rad.}} = A_{\text{rad.}} \epsilon_{\text{rad.}} \times V \times t, \quad (7.4)$$

with $V = 15.3 \text{ m}^3$ the tracker volume, and where $A_{\text{rad.}}$ represents this time a volumic activity, given in Bq/ m^3 .

All these equations, similarly as Eq. (7.1), are valid for a given energy range $[E_{\text{min}}; E_{\text{max}}]$. To find the best energy interval, that is to say the one maximising the limit on $T_{1/2}^{0\nu}$, we must vary E_{min} and E_{max} .

As can be seen in Fig. 7.1, beyond a certain value in energy, the number of background events becomes negligible. Indeed, the ^{208}Tl background dominates at these energies, where it do not exceed one count for $E > 3.2 \text{ MeV}$. This is why the upper limit E_{max} of the energy interval has only a limited impact on the search for the best ROI. It is then natural to study mainly the influence of the lower limit E_{min} . Therefore, the selection efficiencies, entering in the calculation of $T_{1/2}^{0\nu}$ upper limit through the Feldman-Cousins statistics, are presented in Fig. 7.2, as a function of $E > E_{\text{min}}$. We remind a selection efficiency ϵ is the ratio of the number

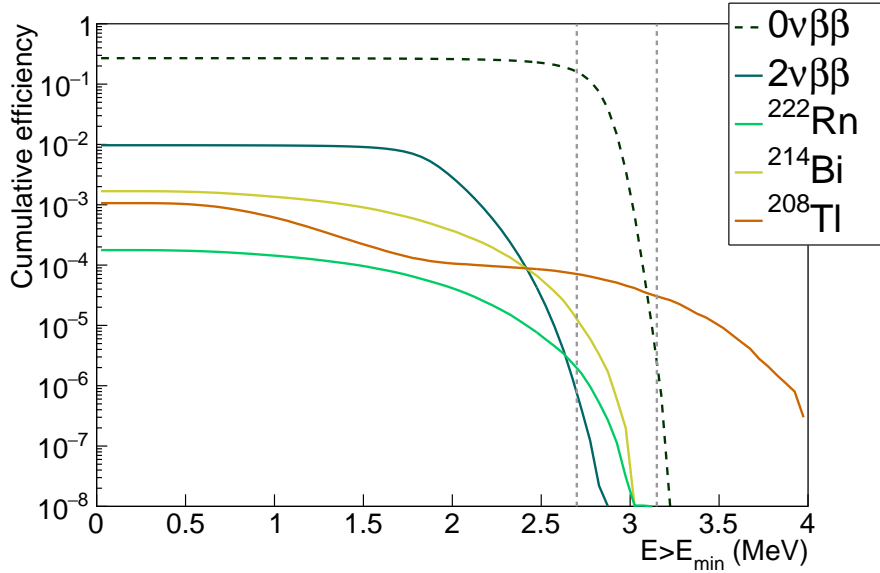


Figure 7.2: Efficiency spectra as a function of $E > E_{\text{min}}$, for the $0\nu\beta\beta$ signal (dashed black line) and for the main backgrounds (plain lines). The two vertical grey lines represent the final ROI optimised for the case of the demonstrator, taken the specified isotope activities.

of selected events, to the number of simulated events. As a matter of fact, we look for an energy region where $\epsilon_{0\nu}$ is high, and where selection efficiencies for the background are low. This choice will directly determine the best value for

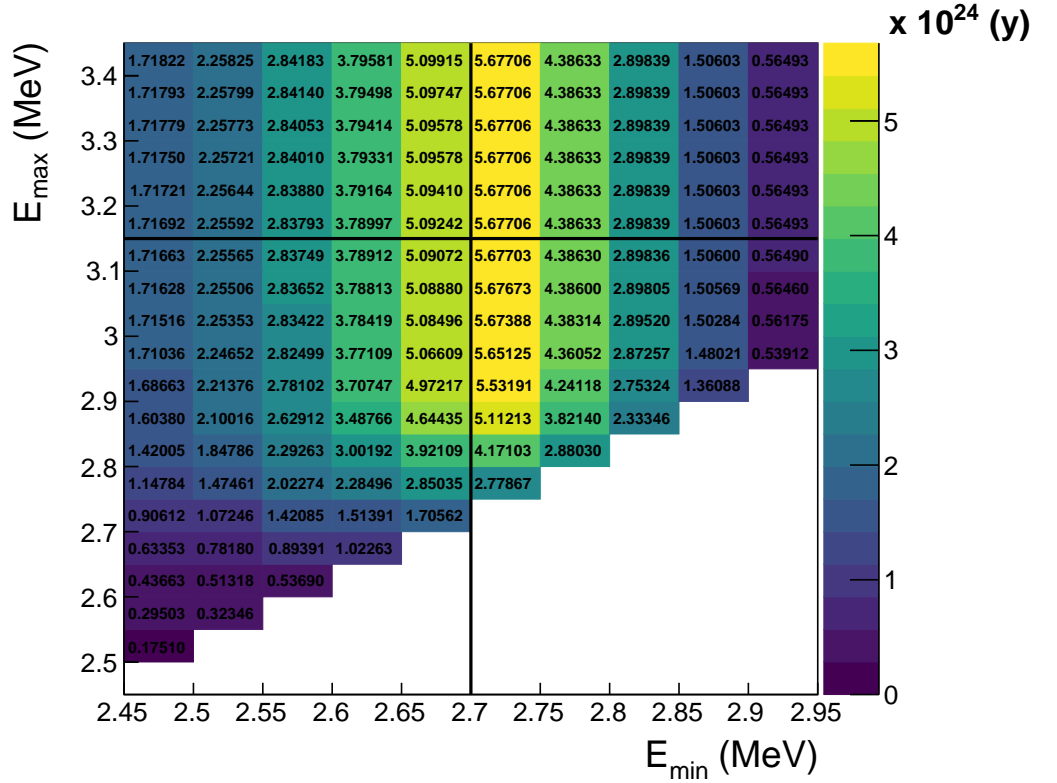


Figure 7.3

$T_{1/2}^{0\nu}$ (90% CL), whose variation as a function of E_{\min} and E_{\max} are presented in Fig. 7.3. As we said, the energy range chosen as the region of interest for the search of the $0\nu\beta\beta$ decays is the one maximising the $T_{1/2}^{0\nu}$. We found that, for the demonstrator exposure, with ^{82}Se sources, with a 25 G magnetic field, and for the specified background activities, the best ROI is $[2.7; 3.15]$ MeV. In this optimised energy range, the sensitivity expected for the SuperNEMO demonstrator stands at

$$T_{1/2}^{0\nu} > 5.68 \times 10^{24} \text{ y} \quad (90\% \text{CL}). \quad (7.5)$$

This result is compatible with the previous analysis lead by Steven Calvez [9].

In this section, we presented the general procedure leading to an optimised result on the $T_{1/2}^{0\nu}$ limit. Thereafter, we discuss the results obtained for different detector exposures (demonstrator and final detector), and different internal background activities. Also, and this is the main purpose of this study, we discuss the influence of the presence of the magnetic field on the final detector's sensitivity.

7.4 Impact of sources contamination levels on the sensitivity

In Sec. 7.3, we gave the best limit on $T_{1/2}^{0\nu}$, driven by Eq. (7.1), for the demonstrator case. In the current section, we study several parameters that could greatly

influence the final result on $0\nu\beta\beta$ sensitivity. The first parameter we will focus on is the level of isotope contaminations (inside the source foils, as well as on the tracker's wires). Secondly, we will evaluate the influence of the 25 G magnetic field on the final sensitivity result that has been given.

7.4.1 Influence of the contamination levels

Specified contamination levels have been established in order to achieve the $0\nu\beta\beta$ half-life target of $\sim 1 \times 10^{26}$ years for the final detector. The ^{82}Se demonstrator source is segmented in 34 foils, whose production was the responsibility of different laboratories (Dubna, LAPP and Tomsk). The sources have undergone different purification treatments, in order to compare them with those of NEMO-3. After the sources production, preliminary measurements have been performed with the BiPo-3 detector to determine the actual ^{208}Tl and ^{214}Bi contamination levels inside the foils [19]. The level of radon emissions inside the tracker was also measured by the collaboration, for each of the four sections of the chamber, using a concentration line. We summarise all these averaged contamination levels in Tab. 7.2, and give a comparison with the detector specifications. We

	Specified activities	Measured activities
^{208}Tl	$2 \mu\text{Bq.kg}^{-1}$	$54 \mu\text{Bq.kg}^{-1}$
^{214}Bi	$10 \mu\text{Bq.kg}^{-1}$	$< 290 \mu\text{Bq.kg}^{-1}$
^{222}Rn	0.15 mBq.m^{-3}	$0.15 \pm 0.02 \text{ mBq.m}^{-3}$

Table 7.2: Real and targeted specified activities for the SuperNEMO detector. The ^{222}Rn tracker contamination is measured with a concentration line [20], extrapolated with a $2 \text{ m}^3/\text{h}$ flow rate. The limit on ^{214}Bi contamination is provided by BiPo measurements for a 90% CL [19].

notice the targeted ^{208}Tl level is not reached, being almost 27 times higher than expected. Nevertheless, in average, a factor of two was gained between the NEMO-3 ^{100}Mo sources and the ^{82}Se sources from the demonstrator. In addition, valuable information has been accumulated on the different production techniques, which are of great importance for the final detector construction. The two best ^{208}Tl source activities were reached by inverse chromatography, encouraging for further investigations in this direction. The sensitivity of BiPo detector only allowed to give an upper limit on the level of internal ^{214}Bi . Precise measurements are expected from the demonstrator calibration. Radon emissions from the tracker were also measured, and extrapolated with an air flow rate of $2 \text{ m}^3/\text{h}$ inside the tracker, showing the targeted level of 0.15 mBq.m^{-3} was reached. We give in the following the influence of the contamination levels on the demonstrator's sensitivity to the $0\nu\beta\beta$ decay.

In Sec. 7.3, we developed the general procedure allowing to set a 90% confidence interval limit on $T_{1/2}^{0\nu}$. For the demonstrator, supposing the specified activities are reached, the demonstrator would achieve a sensitivity of 5.68×10^{24} years on the searched decay, in 2.5 years of data taking, with 7 kg of ^{82}Se . This sensitivity could

be affected by the level of contaminations, measured by BiPo, inside the source foils. We expose in Fig. 7.4 the $T_{1/2}^{0\nu}$ limit as a function of the contamination levels, as well as the corresponding ROI. Four distinct levels of internal contaminations

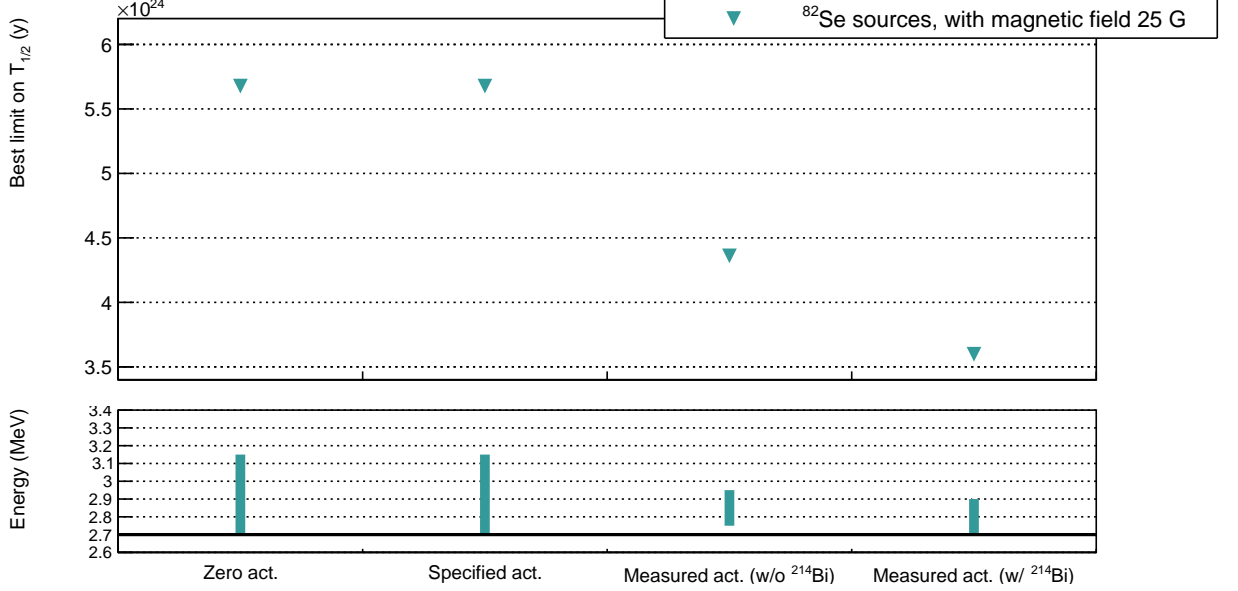


Figure 7.4: The 90% CL limit on the $0\nu\beta\beta$ half-life (top pad), and the corresponding ROI (bottom pad), as a function of the contamination level considered. For the *zero activities* case, we consider hypothetical contamination levels where $\mathcal{A}^{\text{Bi}} = \mathcal{A}^{\text{Tl}} = 0$ Bq/kg. The *specified activities* are presented in Tab. 7.2. The *measured activities*, provided by the BiPo detector [19], are presented in the same table. We consider successively a null ^{214}Bi contamination (*measured act. w/o ^{214}Bi*), or equals to the $290\mu\text{Bq/kg}$ upper limit (*measured act. w/ ^{214}Bi*).

are considered:

- the *zero activities* case, a hypothetical case where the source foils and the tracker are non contaminated at all,
- the *specified activities* case, where the targeted level of contaminations are considered,
- the two *measured* cases, that take into account the measured levels of contaminations at 90% CL. As the ^{214}Bi activity is provided by BiPo measurements as an upper limit, it is possible for this level to be lower than $290\mu\text{Bq/kg}$. So we present the results either considering a zero (*without ^{214}Bi*) or $290\mu\text{Bq/kg}$ (*with ^{214}Bi*) activity.

Regarding at the two first cases, no difference between the best $T_{1/2}^{0\nu}$, nor between the region of interests, is observed. This is explained by the Feldman-Cousins statistics employed to determine the number of expected signal events, given the number of observed background events. When the expected number of background events is negligible (which is the case here), the probability p to observe n_s events,

expecting s signal events is given by a Poisson distribution

$$p = \frac{e^{-s} s^{n_s}}{n_s!}. \quad (7.6)$$

If no background event is observed - and this is assumed to put an upper half-life limit - then $p = e^{-s}$. We can set an upper limit on the expected signal yield s excluding values of s for which $p < \alpha$, here considering $\alpha = 10\%$ ($1 - \alpha = 90\%$ CL). The upper limit for a negligible expected number of background and no signal events observed is therefore $s \leq 2.303$ (90% CL). A direct consequence is, considering that the background levels for the two first cases are negligible, they both reach this limit on the expected number of signal events.

We focus now on the two last contamination cases, for which the measured natural isotope activities are used to determine the best limit on $T_{1/2}^{0\nu}$. For the case where we consider the foils are non contaminated by the ^{214}Bi isotope, a decrease in sensitivity is observed, compared with the ideal zero activities case. If we now apply the $290 \mu\text{Bq/kg}$ upper limit, the level of total internal contaminations is no more negligible, and influence greatly the value of $T_{1/2}^{0\nu}$, decreasing the experiment's sensitivity by a factor 1.5. *Partie à finir*

In the next part, we explore different event selection techniques, with the aim of maximizing the signal-to-background ratio, and thus maximizing the limit on $0\nu\beta\beta$ half-life.

7.4.2 Optimisation of the event selection

The measured level of ^{208}Tl isotope inside the source foils is greater than expected. Moreover, only an upper limit has been set by the BiPo detector regarding the internal ^{214}Bi level. Thus, we aim to set specialised event selections, specially adapted to the measured internal contamination levels.

Most of the double beta experiments are only sensitive to the total electron energy sum. The unique SuperNEMO tracko-calor technology confers the experiment the ability to individually characterise particles (individual energies, emission angles...) By relying on these additional observables, *topological cuts* have been set up, in addition with the basic first order cuts described in Sec. 7.2. These topological cuts are designed to reject events where the two electrons are not emitted simultaneously, or from the same location on the source foils.

The internal probability Based on time-of-flight (TOF) computation, is derived from the internal χ^2 (see details in Sec. 4.1.1). In Fig. 7.5 are presented the internal probability spectra for the $0\nu\beta\beta$ signal and all background processes, after the first order cuts selections. The internal probability distributions for the $0\nu\beta\beta$ and $2\nu\beta\beta$ processes follow the expected flat distribution for electrons emitted simultaneously from the source. The ^{208}Tl and ^{214}Bi distributions are also flat. However, the ^{208}Tl distribution is distorted at low internal probabilities. This might be explained by the existence of a metastable excited state ($\tau_{1/2} = 294\text{ps}$) of the daughter nuclei, which would slightly delay the second electron emitted via internal conversion. This feature will be addressed in detail in Chap. 8. The Radon,

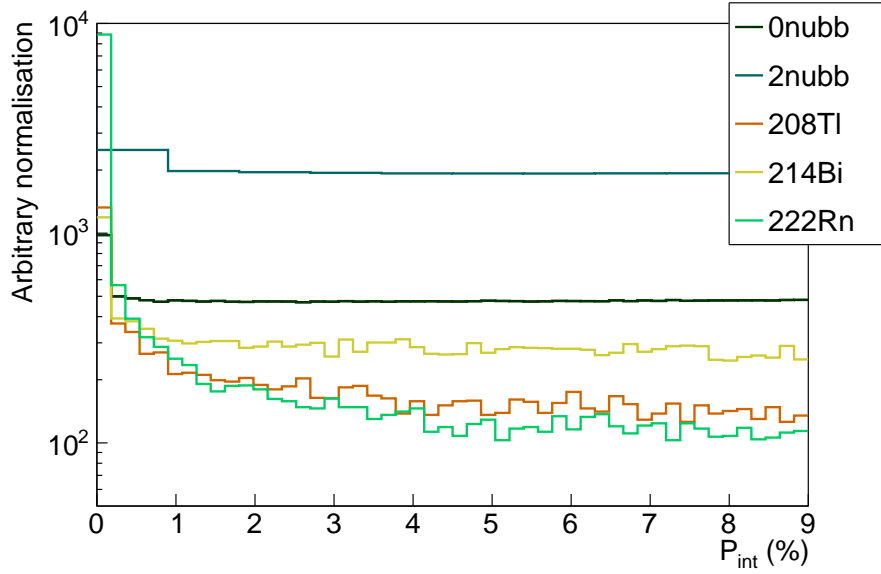


Figure 7.5: Internal probabilities for all processes. First order cuts have been applied.

being a non-internal background, presents a peak at low internal probabilities. Looking at its influence on the final sensitivity, we will establish the most adequate internal probability cut-off, insuring that non simultaneous emitted electrons are rejected.

In Fig. 7.6, we look at the $T_{1/2}^{0\nu}$ best limit set, as a function of the internal probability cut-off applied on the simulated processes. We explore the influence

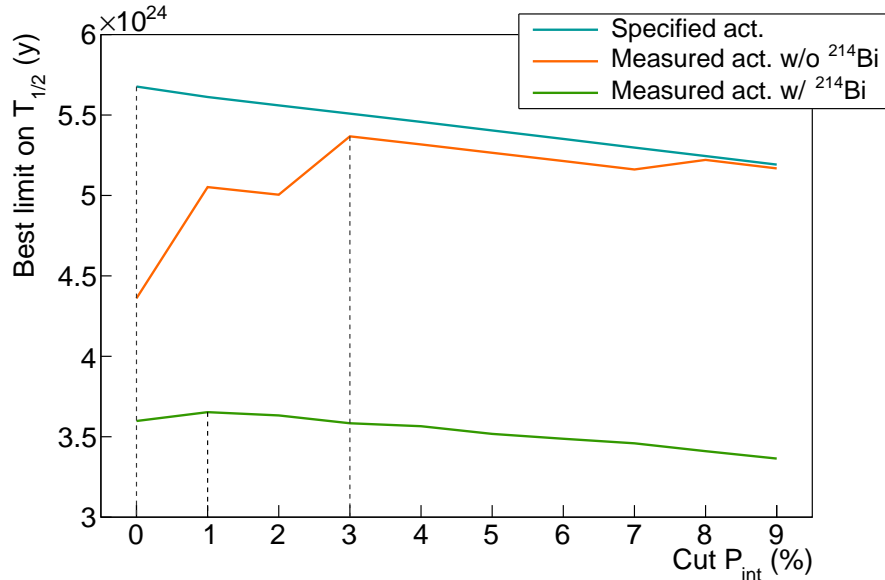


Figure 7.6: Best limit set on $T_{1/2}^{0\nu}$ at 90% CL, as a function of the cut-off applied on internal probability.

of the cut-off for each of the three contamination levels detailed in the previous

subsection. The sensitivity displayed for a 0% cut-off corresponds to the results displayed in Fig. 7.4. With background constraints as low as the specified activities, the internal probability cut-off only decreases the sensitivity to the $0\nu\beta\beta$ decay. Paradoxically, the internal probability cut-off worth it only if there is enough background to be rejected. We are starting to see the usefulness of this cut-off if we take into account the measured activities. An improvement of the sensitivity is obtained for levels ranging from 0 to 3%, the maximum being reached at 3%. If now we take the upper limit for radon contamination, we have to apply a very low cut-off of 1%, to improve slightly the sensitivity. Tab. 7.3 summarizes the best internal probability cut-off to be applied, as well as the corresponding sensitivity achieved. Now that for each activity case, the best cut-off in internal probability

Activity	P _{int} cut-off	$T_{1/2}^{0\nu}$ (90% CL)
Specified	0%	5.68×10^{24} y
Measured w/o ^{214}Bi	3%	5.37×10^{24} y
Measured w/ ^{214}Bi	1%	3.65×10^{24} y

Table 7.3: The optimisation of internal probability selection is presented for each internal background case, and the corresponding limit on $T_{1/2}^{0\nu}$ at 90% level is given.

has been determined, we set out to study the impact of the cut-off on the distance between vertices.

Vertices distance With the track reconstruction, we have access to the coordinates of the reconstructed vertices on source foils. We can use this information in order to maximise the 2ν decays to be selected, while rejecting natural isotope disintegrations. Fig. 7.7 shows the distributions of distance between vertices for each process studied. The two electrons of $0\nu\beta\beta$ and $2\nu\beta\beta$ decays are actually emitted from the same vertex, unlike natural isotope disintegrations. * a finir*

Fig. 7.8 displays the limit set on $T_{1/2}^{0\nu}$ as a function of the applied cut-off on the vertex distance in the Z direction. For all three contamination levels, we reach a plateau for a cut-off of more than 60 mm in Δz . The same conclusions apply to the Δy cut-off. These results are consistent with the findings of the previous analysis conducted by Steven Calvez, asserting the two reconstructed vertices on source foils should not be separated by more than 60 mm horizontally ($|\Delta y| < 60$ mm), and by more than 70 mm vertically ($|\Delta z| < 70$ mm).

These cuts follow the NEMO-3 analysis on the background rejection, whose effectiveness were lately confirmed for the SuperNEMO demonstrator [15]. First order and topological cuts have efficiencies of selection differing for each type of decay. We computed these efficiencies, presented in Tab. 7.4. We observe topological cuts allow the selection of a high proportion of $0\nu\beta\beta$ signal events, while rejecting most of the background events, especially the Radon-induced ^{214}Bi decays inside the tracker.

After looking at the effect of contaminations on the sensitivity, we review the influence of the magnetic field inside the detector.

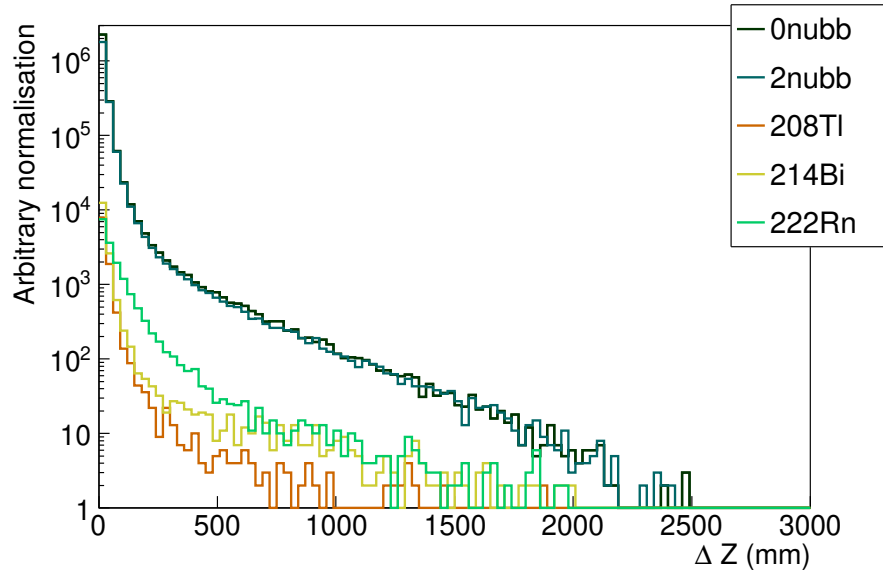


Figure 7.7

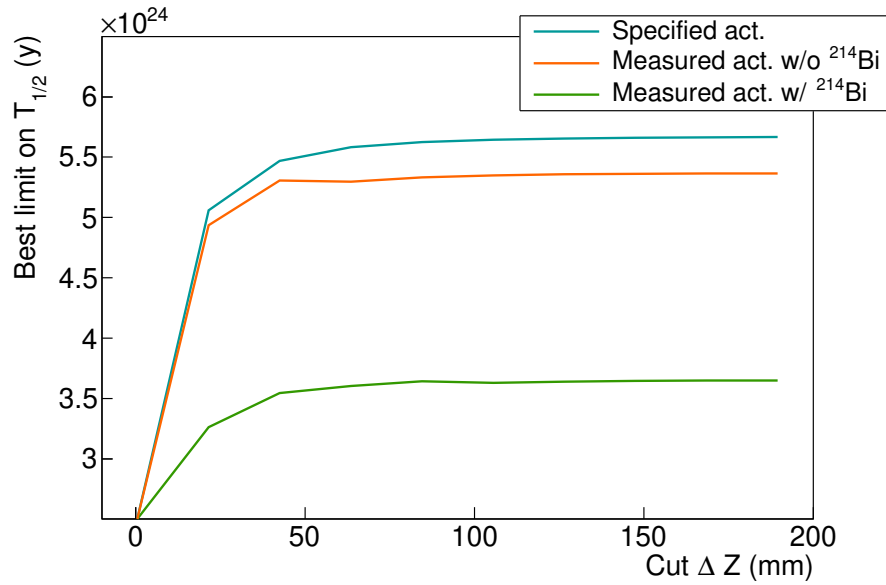


Figure 7.8

- The conclusions about the influence of the contamination levels are valid both for the 25 G or zero magnetic field.
- Parler des cuts topos qui dégradent la sensibilité, pcq artificiellement : parler de la dégradation de la demie vie par les coupures topos quand pas “assez” de bdf

	First order cuts (%)	Internal probability (%)	Vertex distance (%)
$0\nu\beta\beta$	26.9	25.3	24.2
$2\nu\beta\beta$	9.16	8.57	8.01
^{208}Tl	0.106	0.0888	0.0821
^{214}Bi	0.168	0.151	0.140
^{222}Rn	0.0169	7.3×10^{-5}	4.27×10^{-5}

Table 7.4: Number of selected $2e$ topologies compared with the total number of simulated decays, for first order cuts and topological cuts.

7.5 Influence of the magnetic field

As described in Sec. 7.6, the presence of a magnetic field of 25 G could influence the optical modules performances. In the simulated detector, such effects are not yet implemented, therefore can't be observed in the framework of this analysis. However, possible degradation of the event reconstruction efficiency.

We oppose in Fig. 7.4 the $T_{1/2}^{0\nu}$ results with and without this field inside the detector. A third result is also presented, with the mapped field.

7.6 The 25 Gauss magnetic field

As detailed in Sec. 7.6, the SuperNEMO demonstrator was originally designed with a copper coil, similarly to NEMO-3, delivering a magnetic field inside the tracker volume, aiming to provide an electron/positron discrimination by fitting the curved particle tracks by an helix. Studies have been lead to evaluate its influence on the optical modules and on the event reconstruction [9][17].

7.6.1 Influence of the magnetic field on optical modules and reconstruction efficiency

SuperNEMO PMTs are protected from the external magnetic field by an iron shield. Unfortunately, the latter do not perfectly protect the PMTs, and a residual magnetic field is measured inside the shieldings, leading to charge losses and worsened energy resolution. It was shown that applying a 25 G magnetic field, and protect the PMTs with iron magnetic shields would be optimal, but not without consequences. In fact, for the recommended value of 25 G for the magnetic field, PMT charge losses would be close to 8%, and the PMT energy resolution would be increased of $\sim 3\%$. Moreover, the PMTs shieldings could themselves severely impact the shape of the field lines, as well as its strength. In fact, with a 25 G magnetic field generated by the copper coil, the magnetic shields are responsible for the field strength decreasing, and barely 10 G is expected near the source foils. Moreover, the magnetic field strength decreases quickly as we get closer to the calorimeter walls. The reconstruction efficiency could therefore be greatly impacted: the magnetic field intensity varying from the source foils to the

calorimeter wall, electrons trajectory curvatures are not constant, and the track is less well fitted. This effect is higher as the electron energy decreases.

Despite the fact that magnetic shields were designed and installed to protect the PMTs, this field can have a great impact on the calorimeter detection efficiency, and thus could degrade the detector's sensitivity to the $0\nu\beta\beta$ decay. If the studies cited have evaluated the influence of the presence of the magnetic field on the reconstruction efficiency of $0\nu\beta\beta$ events, it remains to be seen its consequences on the final demonstrator sensitivity.

7.6.2 Simulations of the magnetic field inside the demonstrator and reconstructed track fit

In order to study the influence of the magnetic field on the Selenium-82 $0\nu\beta\beta$ sensitivity, the simulations and reconstructions of decays described in Sec. 7.1 have been performed in three different conditions:

- simulations where the magnetic field is turned off,
- simulations with a 25 G *uniform* magnetic field (following recommendations [9]),
- simulations with a 25 G *mapped* magnetic field, taking into account more realistic variations of the magnetic field inside the detector [18].

Each magnetic field conditions have the same number of simulated events, as summed up in Tab. 7.1. Depending on the case considered, the electrons will not have the same trajectory curvature. In the first no-field case, the motion of an electron is in a straight line. The fitting algorithm have thus be modified to match line trajectories. In the second uniform-field case, the best track fit is performed by helices. Finally, the best tracking option (line or helix) for the third mapped-field will be discussed in the next section.

- avec variation coupure énergie
- Parler du champ non uniforme/attenuation

7.7 Searching for the Neodymium-150 $0\nu\beta\beta$ decay

This study was conducted jointly with the PhD student Axel Pin, from CENBG []. Although we both worked on the whole of the analysis, I presented in detail, in the previous sections, the results regarding the influence of the magnetic field. Meanwhile, Axel Pin will present in detail the possibility of changing the Selenium material by Neodymium sources [21]. The current section aims at summarise the feasibility study on Neodymium sources.

In the case SuperNEMO demonstrates the feasibility of a large-scale tracko-calo experiment, we would examine the possibility of different source isotopes, as done on NEMO-3. In this framework, we present here the sensitivity of SuperNEMO to the $0\nu\beta\beta$ of Neodymium-150. The ^{150}Nd has a more favourable $Q_{\beta\beta}$ than ^{82}Se , with $Q_{\beta\beta} = 3.37$ MeV, . However, its $T_{1/2}^{2\nu}$ is lower, with 9.1×10^{18} years [ref]. For this study, we keep the ^{82}Se values for the contaminations, despite different purification efficiencies for the two isotopes.

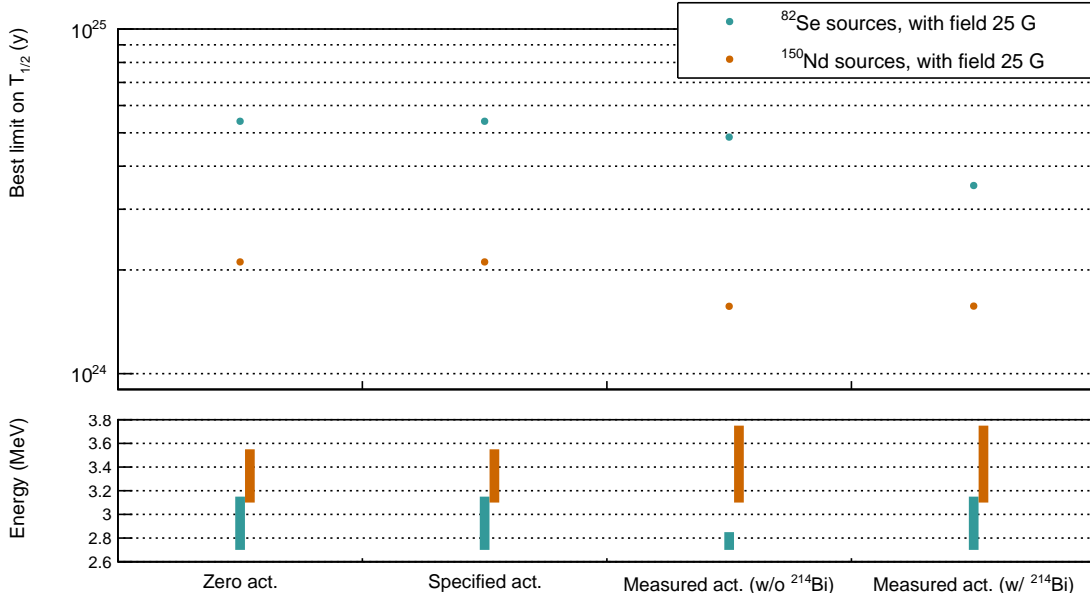


Figure 7.9: Best limit set on $0\nu\beta\beta$ half-life (top pad), and the corresponding ROI (bottom pad), as a function of the contamination level considered, considering ^{150}Nd sources and an exposure of 17.5 kg.

- préciser que compte-tenu du Z important du ^{150}Nd , même si la demi-vie de la 2ν est assez faible, cela ne gêne pas trop car les effets coulombiens font que la 2ν ne contribue pas trop à haute énergie.
- distribution $t_{1/2}$ avec différents échantillons de simus (17.5 kg.y)

7.8 The final detector sensitivity

The final goal of the SuperNEMO demonstrator is to demonstrate that the NEMO technology is scalable to reach high half-life sensitivity on the $0\nu\beta\beta$ decay. It was therefore mandatory to study the case of the final detector sensitivity, consisting in building 20 modules similar to the SuperNEMO demonstrator, to reach unprecedented levels on effective neutrino masses.

7.9 Conclusion

- Etude plus générale avec bkg externe+lab (reprendre chiffres NEMO3) + neutrons (cf NEMO3)
- Plot général récap tous résultats
- delayed cells- γ improvement, cf NEMO 3
- ouverture sur possibilité d'étudier l'influence de la résolution en temps des PMs sur l'eff des coupures (Pint)
- cellules tracker dead- γ refaire analyse
- manque de stat pour le neodyme car ROI haute E
- légères diff avec résultats axel car légères diff dans sélections d'ev car utilisation PID
- tenir compte de la dégradation en énergie dans les simus du au B

Bibliography

- [1] M. et al. Agostini. Probing majorana neutrinos with double- β decay. *Science* 365, 1445, 2019.
- [2] S.I. et al. Alvis. Search for neutrinoless double-beta decay in ^{76}Ge with 26 kg-yr of exposure from the majorana demonstrator. *Phys. Rev. C*, 100, 2019.
- [3] O. et al. Azzolini. First result on the neutrinoless double- β decay of ^{82}Se with cupid-0. *Phys. Rev. Lett.*, 120:232502, Jun 2018.
- [4] C. et al. Alduino. First results from cuore: A search for lepton number violation via $0\nu\beta\beta$ decay of ^{130}Te . *Phys. Rev. Lett.*, 120:132501, Mar 2018.
- [5] J. B. et al. Albert. Search for neutrinoless double-beta decay with the upgraded exo-200 detector. *Phys. Rev. Lett.*, 120:072701, Feb 2018.
- [6] A. et al. Gando. Search for majorana neutrinos near the inverted mass hierarchy region with kamland-zen. *Phys. Rev. Lett.*, 117:082503, Aug 2016.
- [7] Nucleid database.
- [8] R. et al. Arnold. Probing new physics models of neutrinoless double beta decay with supernemo. *Eur. Phys. J. C*, 2010.
- [9] S. Clavez. *Development of reconstruction tools and sensitivity of the SuperNEMO demonstrator*. PhD thesis, Université Paris Sud, 2017.
- [10] Gomez-Cadenas et al. Physics case of supernemo with ^{82}Se source. Internal presentation, 2008.
- [11] R. et al. Arnold. Final results on ^{82}Se double beta decay to the ground state of ^{82}Kr from the nemo-3 experiment. *Eur. Phys. J. C*, 2018.
- [12] Tretyak V.I. Ponkratenko O.A. and Zdesenko Yu.G. The event generator decay4 for simulation of doublebeta processes and decay of radioactive nuclei. *Phys. At. Nucl.*, 63:1282–1287, Jul 2000.
- [13] Perrot F. Radiopurity measurements for 8" pmts and preliminary budget for the sn demonstrator. Internal presentation, 2017.

- [14] R. et al. Arnold. Results of the search for neutrinoless double- β decay in ^{100}mo with the nemo-3 experiment. *Phys. Rev. D*, 2015.
- [15] Steven Calvez. Updates on the demonstrator sensitivity and radon study. Internal presentation, 2014.
- [16] Cousins D. Feldman G. A unified approach to the classical statistical analysis of small signals. *Phys.Rev.*, pages 3873–3889, 1999.
- [17] Garrido X. Bongrand M. Hamamatsu 8” pmt test in magnetic shield. Internal presentation, 2014.
- [18] Snow S. A magnetic field map for the tracker. Internal presentation, 2015.
- [19] Loaiza P. Source foils measurement with bipo. Internal presentation, 2017.
- [20] Xin Ran Liu. Radon mitigation strategy and results for the supernemo experiment. IoP APP / HEPP Conference, 2018.
- [21] A. Pin. *Recherche de la nature du neutrino via la décroissance double bêta sans émission de neutrinos. Caractérisation et optimisation du calorimètre SuperNEMO et impact sur la recherche de la décroissance du ^{82}Se* . Développement du premier prototype LiquidO. PhD thesis, Université Bordeaux-Gradignan, 2020.